

## Calibration of ACS Prism Slitless Spectroscopy Modes

S. S. Larsen, M. Kümmel and J. R. Walsh

*ESO/ST-ECF, Karl-Schwarzschild-Str. 2, D-85748 Garching bei München,  
Germany*

**Abstract.** The Advanced Camera for Surveys is equipped with three prisms in the Solar Blind (SBC) and High Resolution (HRC) Channels, which together cover the 1150 – 3500 Å range, albeit at highly non-uniform spectral resolution. We present new wavelength- and flux calibrations of the SBC (PR110L and PR130L) and HRC (PR200L) prisms, based on calibration observations obtained in Cycle 13. The calibration products are available to users via the ST-ECF/aXe web pages, and can be used directly with the aXe package. We discuss our calibration strategy and some caveats specific to slitless prism spectroscopy.

### 1. Introduction

The Advanced Camera for Surveys is currently the only instrument on HST which provides spectroscopy in the UV-optical range. With STIS being unavailable (at least for the moment), the interest in the ACS spectroscopic modes has increased substantially. An extensive calibration effort was undertaken in Cycle 13 in order to provide much improved wavelength- and flux calibrations for the prism modes which had seen little use in earlier cycles. The ACS has two prisms (PR110L and PR130L) installed in the Solar Blind Channel (SBC), both covering the wavelength range from roughly 1200Å – 2000Å. The main difference between the two SBC prisms is that the sensitivity of PR110L extends below the geocoronal Ly  $\alpha$ , while that of the PR130L does not. The sensitivity below 1216 Å results in a significantly higher sky background for the PR110L. The one prism (PR200L) in the High Resolution Channel covers the range  $\sim$  1800Å– 3500Å. In this paper we present the calibration observations and discuss the derived trace-, wavelength and flux calibrations. The calibrations presented here are implemented in configuration files for the aXe package (Kümmel et al., these proceedings) and are made available to users via the aXe web pages (<http://www.stecf.org/software/axe>).

Spectroscopic observations with the ACS prisms share many similarities with the G800L grism in the WFC and HRC channels, but there are also some differences. In both cases the object spectrum (or spectra) may fall anywhere on the detector, and the reference point for the wavelength scale is typically established using a direct image taken immediately before (or after) the prism exposure. The direct image is even more crucial for the prism modes, which do not show a zeroth order spectrum (nor any higher- or negative orders). Contrary to the case of grism spectroscopy, the wavelength scale of the prism spectra is highly non-linear, with the spectral resolution decreasing towards longer wavelengths (see below). For the PR200L, this causes a “red pile-up” with wavelengths between 4000 Å and 10000 Å being compressed into only 7 pixels. This pile-up can be particularly troublesome for red objects, where light from the diffraction spikes and outer halo of the PSF may contaminate the bluer parts of the spectrum. These effects are still poorly quantified. No such pile-up is seen for the SBC prisms, due to the lack of sensitivity at wavelengths  $>$  2000Å for the MAMA detector.

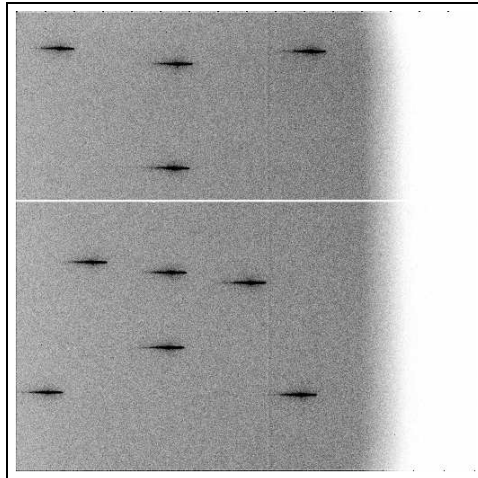


Figure 1.: Sum of the 10 pointings obtained for PG1322+659 for the PR110L. Note the vignetting at the right-hand side of the field. A few dead rows at  $Y \approx 600$  are seen as a horizontal white line.

## 2. Observations

The relatively low spectral resolution of the prisms, particularly at longer wavelengths, and the high spatial resolution of the SBC and HRC cameras limit the choice of suitable wavelength calibrators. The calibration targets must have strong emission features in the ultraviolet spectral region, and at the same time be compact. For the SBC, an additional constraint was the “bright object protection” limit. We eventually settled on a combination of a planetary nebula in the Large Magellanic Cloud (LMC-SMP-79) and a QSO at redshift  $z = 0.836$  (Q0037-3544) for the PR200L, and two QSOs at redshifts  $z = 0.168$  (PG1322+659) and  $z = 0.098$  (PG1404+226) for the SBC prisms. The PN was known from existing STIS spectra to have strong C III] and [C II] emission lines and be relatively compact (though not point-like). The QSOs were selected from the compilation of Véron-Cetty & Véron (2003), which lists 48921 quasars and makes it possible to select a QSO with emission features (Ly  $\alpha$ , C IV etc.) at essentially any desired wavelength. We required the calibration targets to have existing HST spectra (either from FOS or STIS) and low reddenings ( $A_B < 0.1$  mag), but even with these additional constraints it was not difficult to find suitable QSO targets. For the flux calibration we observed two white dwarf standards, WD1657+343 and LDS749B. STIS spectra of these stars were kindly provided by R. Bohlin.

Each target was observed at several positions across the detector in order to map spatial variations in the trace- and wavelength solutions, as well as any large-scale sensitivity variations. For each prism, one wavelength calibration target was observed at 9 or 10 positions (i.e. 2 orbits) and the other at 5 positions (one orbit). The flux standards were observed at 5–6 different positions. Each prism exposure was preceded by a direct image through the F165LP filter (for the SBC) or F330W (for the HRC). The F165LP filter was chosen in order to avoid conflict with the bright object protection limit for the QSO targets. However, for one of the flux standards we obtained direct images in both the F122M and F165LP filters in order to check for any offsets between exposures in the two bands. Such offsets were indeed found (see below).

The coverage of the field is illustrated in Fig. 1, which shows a sum of the 10 PR110L exposures obtained for PG1322+659. The MAMA detector has a few dead rows at  $Y \approx 600$  which show up as a horizontal white line in the figure. To avoid these, the default aperture center is at (512, 400). Note that there is significant vignetting at the right-hand side of the

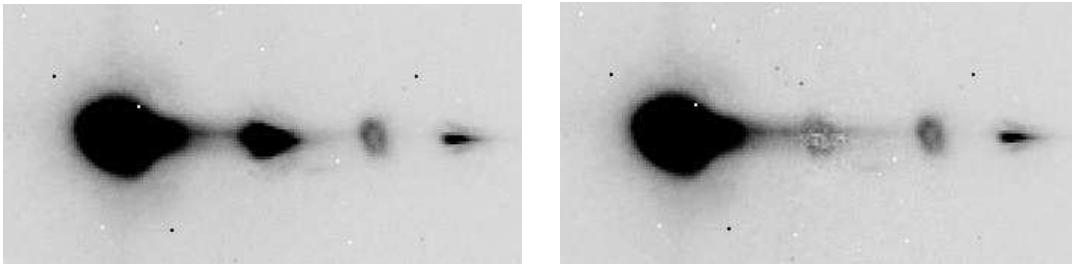


Figure 2.: PR200L image of LMC-SMP-79. Left: raw image, Right: after subtraction of contaminating object. Note that the nebula is resolved at the HRC resolution. From the left to the right, the four main “features” in the spectrum are: the red pile-up, [C II] 2325Å/contaminating star, C III] 1909Å, and another contaminating star.

field, affecting  $\sim 200$  image columns. A similar phenomenon is seen for the HRC/PR200L, but affecting the left-hand side of the field.

A few difficulties were encountered with the data for LMC-SMP-79. First, with a diameter of about  $0''.3$ , the planetary nebula was slightly resolved at the resolution of the HRC. Second, by an unfortunate coincidence the prism spectra of the nebula were contaminated by two stars in the field, one of which affected the [C II] 2325 Å line (Fig. 2). Fortunately, we found that the contaminating object could be removed by scaling and subtracting the spectrum of a star of similar spectral type located elsewhere in the field. This procedure worked well enough that we could recover the [C II] 2325 Å line. Fig. 2 also illustrates the PR200L “red pile-up”, which is the dominant feature at the left (red) end of the spectrum.

### 3. Wavelength- and trace solutions

The spectral trace- and wavelength solutions are defined with respect to a reference position,  $(X_{\text{ref}}, Y_{\text{ref}})$ , which was measured by running the SExtractor code (Bertin & Arnouts 1996) on the direct images. The trace descriptions were then derived by measuring the centroid along the image columns (corresponding to the spatial direction) for the flux standard spectra, and fitting a straight line (for the PR110L and PR200L) or 2nd order polynomial (for PR130L) to the offset  $\Delta Y = Y_{\text{trace}} - Y_{\text{ref}}$  vs.  $\Delta X = X_{\text{trace}} - X_{\text{ref}}$ . In all cases the dispersion direction of the prism spectra was found to be aligned with the image rows to within 1 degree, towards positive  $\Delta X$  for PR200L and negative  $\Delta X$  for the SBC prisms. The variation in the offsets and slopes  $\Delta Y/\Delta X$  of the prism spectra was fitted with 2-dimensional 1st order polynomials as a function of position on the detector (not reproduced here due to space constraints).

Wavelength solutions were assumed to be of the form used by Bohlin et al. (2000), i.e.

$$\lambda = a_1 + \frac{a_2}{(\Delta X - a_0)} + \frac{a_3}{(\Delta X - a_0)^2} + \frac{a_4}{(\Delta X - a_0)^3} + \frac{a_5}{(\Delta X - a_0)^4} \quad (1)$$

where each of the coefficients  $a_0 \dots a_5$  can be a function of  $(X_{\text{ref}}, Y_{\text{ref}})$ . In order to define the wavelength solutions, the prism spectra were first extracted with aXe using a configuration file where the “wavelength” scale was simply the pixel offset,  $\Delta X$ , along the trace. The aXe spectra were then converted to IRAF format, and the  $\Delta X$  values for the various emission lines were measured with the SPLOT task, using a Gaussian fit. We then solved directly for the full, spatially dependent, wavelength solution. In the PN spectrum we could measure the C III] 1909Å and [C II] 2325Å lines and in the spectrum of Q0037-3544 we could measure Ly $\alpha$ , C IV and C III] redshifted to 2233Å, 2844Å and 3503Å, thus providing 5 wavelength sampling points for the PR200L. For the SBC prisms, we detected Ly  $\alpha$  redshifted to 1420Å

Table 1.: Wavelength solution terms

SBC:		PR110L	PR130L
$a_0$		$-95.70 - 0.00662 \times X_{\text{ref}} + 0.01760 \times Y_{\text{ref}}$	$-80.61 - 0.00711 \times X_{\text{ref}} + 0.01547 \times Y_{\text{ref}}$
$a_1$		$1049.39 + 0.02105 \times X_{\text{ref}} - 0.01867 \times Y_{\text{ref}}$	$1072.71 + 0.01249 \times X_{\text{ref}} - 0.01699 \times Y_{\text{ref}}$
$a_2$		$2.11506 \times 10^4$	$-1.49676 \times 10^4$
$a_3$		$9.23749 \times 10^6$	$1.94800 \times 10^6$
$a_4$		$4.93403 \times 10^8$	$5.48481 \times 10^7$
$a_5$		$1.24585 \times 10^{10}$	$1.11636 \times 10^9$

HRC:		PR200L
$a_0$		$145.755 + 0.00872 \times X_{\text{ref}} - 0.01925 \times Y_{\text{ref}}$
$a_1$		$1147.24 - 0.03042 \times X_{\text{ref}} - 0.00782 \times Y_{\text{ref}}$
$a_2$		$8.11002 \times 10^4$
$a_3$		$-8.28929 \times 10^5$
$a_4$		$-4.65350 \times 10^6$
$a_5$		$1.68888 \times 10^8$

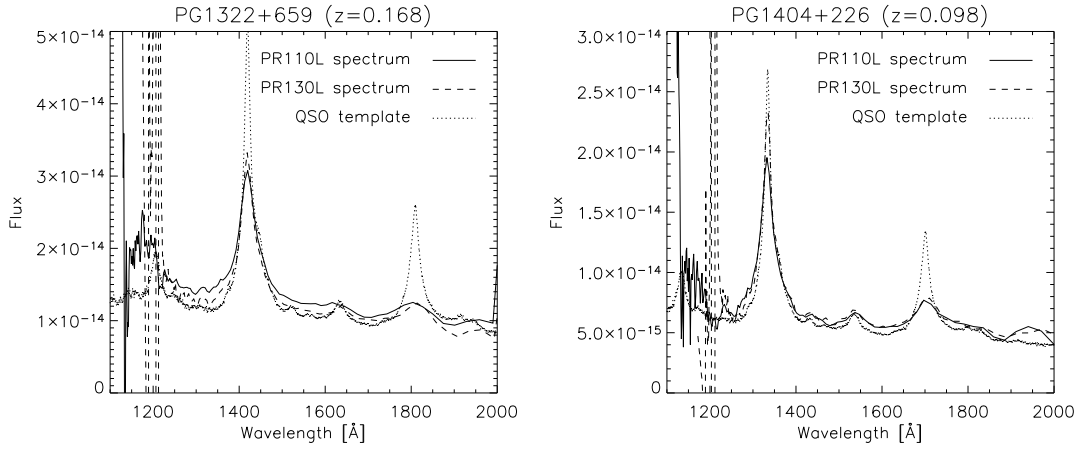


Figure 3.: SBC PR110L and PR130L spectra of PG1322+659 (left) and PG1404+226 (right). A scaled template QSO spectrum (from Zheng et al. 1997) is shown for comparison.

and  $1335\text{\AA}$  in the spectra of PG1322+659 and PG1404+226 respectively, as well as C IV redshifted to  $1701\text{\AA}$  for PG1404+226. The spectra of PG1322+659 had too low resolution at the wavelength of C IV ( $1806\text{\AA}$ ) to allow useful measurements of this feature. Thus, we have 3 wavelength sampling points for the calibration of the SBC prisms. The resulting wavelength solutions are reproduced in Table 1. Note that we have adopted the higher order terms from Bohlin et al. (2000), i.e.  $a_3$ ,  $a_4$  and  $a_5$  for the PR200L, and  $a_2 \dots a_5$  for PR110L and PR130L. However, the  $a_2$  term we derive for the PR200L is quite similar to that derived by Bohlin et al. ( $81100$  vs.  $83000$ ).

The trace- and wavelength solutions derived here assume that direct images are taken in the F165LP filter (for the SBC) or in F330W (for the HRC). For the SBC, images taken in different filters show offsets of up to 12 pixels, so it is important to correct any coordinates measured on images taken in filters other than F165LP for these offsets. A preliminary analysis of these offsets, using our data and data from program 9563 (P.I.: G. De Marchi), suggests that the following corrections should be applied (all in pixels): F115LP:  $(\Delta x, \Delta y) = (-3.74, 12.13)$ ; F122M:  $(\Delta x, \Delta y) = (-3.74, 12.07)$ ; F125LP:  $(\Delta x, \Delta y) = (0.97, -2.44)$ ; F140LP:  $(\Delta x, \Delta y) = (2.88, -8.48)$  and F150LP:  $(\Delta x, \Delta y) = (-0.31, 1.26)$ .

Sensitivity functions were derived for each prism by dividing the prism spectra of the flux standards with the standard STIS spectra, and fitting the ratio with a spline function.

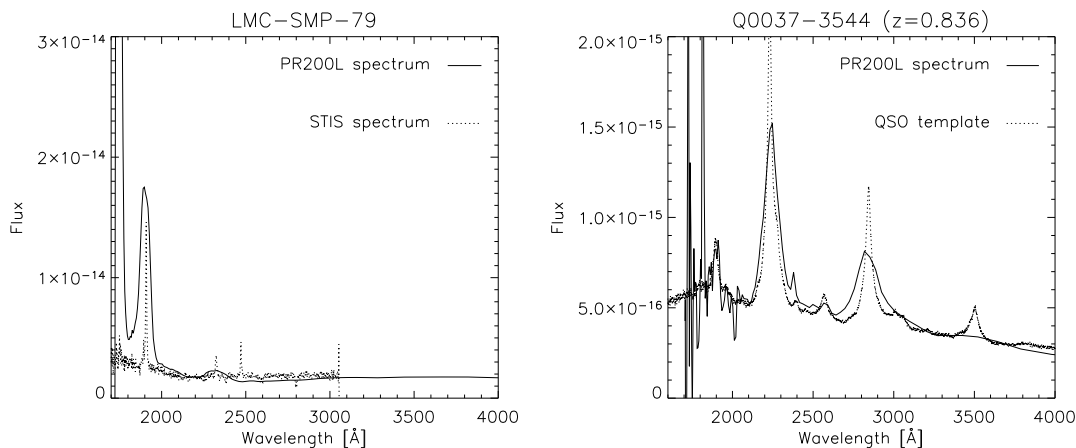


Figure 4.: HRC PR200L spectra of LMC-SMP-79 (left) and the quasar Q0037-3544 (right). For comparison, a STIS spectrum of LMC-SMP-79 (courtesy L. Stanghellini) and a scaled quasar template spectrum are shown.

The spectra of the flux standards were extracted using an extraction box height of  $\pm 0''.5$ . A flatfield cube (Kümmel et al., these proc.) has been defined for the SBC prisms, although not including any wavelength-dependency. This shows sensitivity variations across the SBC detector amounting to a few percent.

#### 4. Consistency checks

Figs. 3 and 4 show the SBC and HRC prism spectra of the wavelength calibration targets, extracted with aXe, compared with a template QSO spectrum (Zheng et al. 1997) and the STIS spectrum of LMC-SMP-79 (courtesy of L. Stanghellini). The QSO template spectrum has been adjusted to the redshift of the corresponding targets and scaled to match the data. No reddening correction has been applied, but the observed QSOs all have  $A_B < 0.1$  mag. The prism observations appear in good agreement with the reference spectra, both as far as the wavelength scales and flux calibrations are concerned. While comparison of aXe-extracted prism spectra of the *flux* standards with the STIS reference spectra shows agreement to about 5%, this agreement may be somewhat deceptive, since the sensitivity files were of course derived from those observations in the first place. The comparison in Figs. 3 and 4 thus provides a welcome independent check, for objects which have rather different spectral energy distributions than the WD standards. While the absolute scalings of the reference spectra here are arbitrary, the overall shape of the prism spectra appears correct, even at longer wavelengths where the wavelength solutions become increasingly uncertain. However, note that the decrease in spectral resolution at longer wavelengths makes it difficult to detect even relatively strong features, such as those seen in the QSO spectra.

The wavelength scale is generally accurate to better than a pixel. The dispersion of the SBC prisms is about  $2 \text{ \AA pixel}^{-1}$  at  $1200 \text{ \AA}$ , but degrades to about  $10 \text{ \AA pixel}^{-1}$  at  $1600 \text{ \AA}$  and  $30 \text{ \AA pixel}^{-1}$  at  $2000 \text{ \AA}$ . The PR200L has a dispersion of about  $5 \text{ \AA pixel}^{-1}$  at  $1800 \text{ \AA}$  and nearly  $40 \text{ \AA pixel}^{-1}$  at  $3000 \text{ \AA}$ . So while the three prisms together cover the full wavelength range from  $1150 \text{ \AA}$ –  $3500 \text{ \AA}$ , the spectral resolution is highly non-uniform.

Using the sensitivity curves derived here, we can calculate the total system throughput for each prism, as shown in Fig. 5. The PR200L reaches a peak efficiency of about 10%, while the SBC prisms peak at 3–4%. These estimates are simply the measured count

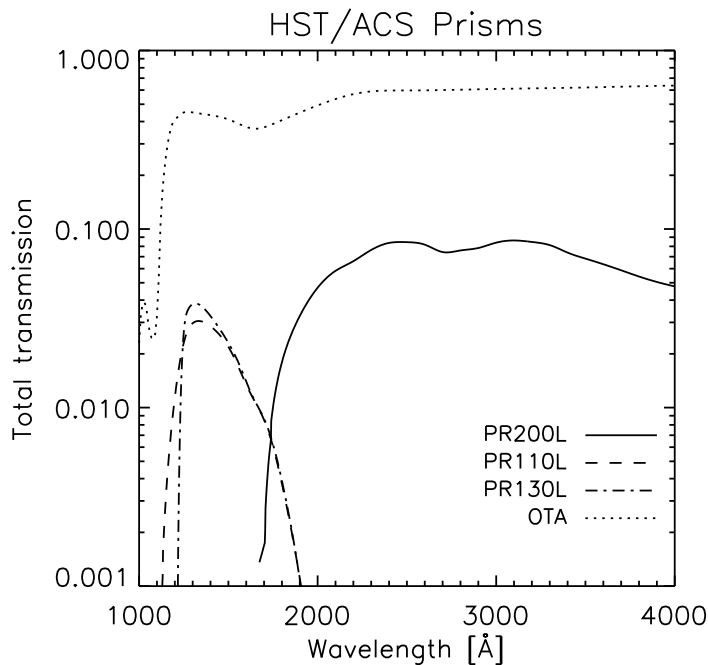


Figure 5.: Total transmission of the ACS prisms relative to the “perfect telescope”, based on the sensitivity curves derived here. The dotted line indicates the throughput of the OTA.

rates vs. the maximum possible rates, assuming a telescope aperture of  $4.52 \text{ m}^2$ , and the throughput curves thus include all the effects of mirror coatings, detector sensitivity etc. For comparison, the throughput of the Optical Telescope Assembly (OTA) alone is also shown.

## 5. Summary

The SBC and HRC prisms are now fully calibrated, both in wavelength and flux. The calibration products are available for use with the aXe package, and can be downloaded from the aXe web pages. Future calibration observations will aim to monitor the stability of the prism modes and possibly provide various improvements, such as quantifying the effect of scattered light from the red pile-up in the PR200L. A better understanding of the general properties of the SBC and HRC detectors, such as CTE effects, may also lead to improvements in prism spectroscopy.

## References

- Bertin, E., & Arnouts, S., 1996, *A&A Suppl.*, 117, 393  
 Bohlin, R. C., Hartig, G., & Boffi, F. R., 2000, ACS Instrument Science Report ISR 00-01  
 Véron-Cetty, M. P., & Véron, P., 2003, *A&A*, 412, 399  
 Zheng, W., Kriss, G. A., Telger, R. C., Grimes, J. P., & Davidsen, A. F., 1997, *ApJ*, 475, 469